Chapter 13

Combustion Processes in Interfacial Instabilities

Praveen Ramaprabhu, Nitesh Attal and
Hilda Varshochi

Additional information is available at the end of the chapter

http://dx.doi.org/10.5772/64746

Abstract

Fluid instabilities, particularly interfacial instabilities, have proven to be a powerful mechanism in driving and sustaining combustion processes in several devices of practical interest. Modern combustors are in fact designed to exploit the mixing and combustion characteristics associated with a broad class of canonical, interfacial instabilities. In spite of their relevance to combustor design, a detailed understanding of such flows has been elusive. While much progress has been made in gaining insights into the dynamics of shear-driven flows, an understanding of the interaction between combustion processes and other interfacial instabilities remains preliminary. In this chapter, we review recent results on Rayleigh-Taylor (RT) instability and the shock-driven Richtmyer-Meshkov (RM) instability in the context of combustion. The vast catalogue of research on non-reacting RT and RM flows has demonstrated these instabilities can be manipulated to achieve more efficient and aggressive mixing in comparison with the canonical Kelvin-Helmholtz (KH) problem. This has motivated recent efforts to understand RT/RM instability development in the presence of chemical reactions, leading to combustion and heat release – we present a review of these results and identify opportunities and challenges in this chapter.

Keywords: interfacial instabilities, Rayleigh-Taylor instability, Kelvin-Helmholtz instability, Richtmyer-Meshkov instability, non-premixed combustion modelling

1. Introduction and background

Turbulent mixing triggered by interfacial instabilities [1–4] is a fundamental process that dominates several engineering applications and natural phenomena. In many instances, the turbulence is profoundly modified by heat release at low or high energy densities, and product

formation from chemical or nuclear reactions. Furthermore, when the mixing occurs across an interface that initially separates a fuel from an oxidizer medium in a non-premixed configuration, the turbulent mixing is a rate-limiting step that dictates the progress of the reactions at the flame site. Thus, the flow affects the flame and vice-versa. In a recent, comprehensive review of turbulent mixing, Dimotakis [5] proposed a hierarchy of mixing phenomena extending from passive scalar mixing (Level-1) to the so-called Level-3 mixing where the active coupling described above is dominant. While such complex interactions are important in describing flow conditions as they exist in engineering applications, the vast majority of turbulence models that seek to obtain reduced order descriptions of the flow assume [6] self-similar, statistically steady, universal behaviour. Thus, reliable data from experiments and simulations is in great demand to verify the validity of these hypotheses, but has not been forthcoming due to challenges in accurately diagnosing these complex flows. The research described herein attempts to break this impasse by performing systematic, high resolution simulations of a new class of idealized flow problems and developing an understanding of the mixing processes based on the data available.

The Kelvin-Helmholtz (KH) instability occurs at a sharp or diffuse interface separating two streams at different velocities, so that the velocity differential ΔU serves to drive the growth of imposed perturbations at the interface. Much of the research on KH instabilities has been motivated by its central role in mixing fuel and oxidizer in several commonly used combustor designs. KH instabilities, whether they occur in a mixing layer, a planar or cylindrical jet, have provided a useful canonical framework for understanding non-premixed combustion. In fact, the design of many modern day combustor devices is acutely informed by the desire to exploit the dynamics of KH-driven mixing between fuel and oxidizer streams. However, there exist alternate combustor designs that exploit the mixing characteristics of other interfacial instabilities such as the RT and shock-driven RM flows. In spite of the importance of these flows in recent combustor designs [7–10], a detailed and comprehensive understanding has not emerged. This is especially true when these flows occur in non-premixed configurations.

We will describe our recent work that addresses a few of the above issues in the areas of reacting RM and RT flows. When a shock wave interacts with a contact discontinuity separating different gases, the material interface is susceptible to the development of the Richtmyer-Meshkov (RM) instability [11–13]. The instability is driven by the deposition by the shock of baroclinic vorticity [14–16] due to locally misaligned density and pressure gradients ($\sim \nabla \rho \times \nabla p$) at the interface. Perturbations present initially at the interface can thus be amplified, first through a phase of linear growth [11, 17], followed by non-linear saturation [18, 19], and eventually turbulent mixing [20]. The non-reacting RM flow has been extensively studied using theory [11, 17–19], simulations [20–25] and experiments [12, 26–30]. However, if the initial sharp interface separates a fuel and oxidizer at elevated temperatures, the turbulent mixing will enable, and in some cases limit, chemical reactions between the reactants resulting in a non-premixed combustion process. Thus, this coupled physics problem provides an idealized test bed for developing a fundamental understanding of turbulent phenomena in the presence of heat addition and product formation due to combustion.

http://dx.doi.org/10.5772/64746

Turbulent mixing and combustion enhanced by RM plays a central role in the performance of scramjets. In most scramjet designs, the interface between the fuel jet and air co-flow is repeatedly shocked by a stationary shock train, so that the misaligned density and pressure gradients result in the deposition of baroclinic vorticity. The induced velocity from the baroclinic vorticity deposition drives much of the subsequent instability development. As a result, the instability growth rate, heat release rate from combustion and combustion efficiency may all be manipulated through the incident shock strength, density ratio between the fuel and oxidizer and initial conditions that seed the interface prior to shock impact.

The dynamics of the shock-interface interaction has been investigated extensively in an idealized framework through a class of shock-bubble problems, which represent the simplest RM configuration. The study of shock interaction with a spherical flame bubble was first undertaken experimentally by Markstein [31] who observed the emergence of an eventual chaotic flame from the deposited baroclinic vorticity. The shock-bubble problem was also investigated theoretically by Picone and Boris [16], who examined the flow resulting from the interaction of a planar shock with a cylindrical flame region. Several numerical studies have also addressed this problem including investigations of shock-flamelet interactions [32, 33], shock interactions with cylindrical jet flames [34] and DDT phenomena in shock-bubble flame interaction [35]. Recently, Haehn et al. [36] performed shock tube experiments in which a focused, spherically converging shock interacted with a spherical bubble consisting of a premixed combination of H_2, O_2 and Xe, so that the high temperatures from the shock heating resulted in combustion and heat release. In **Figure 1(a)**, we show the schematic of an ideal shock-bubble configuration, which we have investigated using careful numerical simulations described in Section 2.

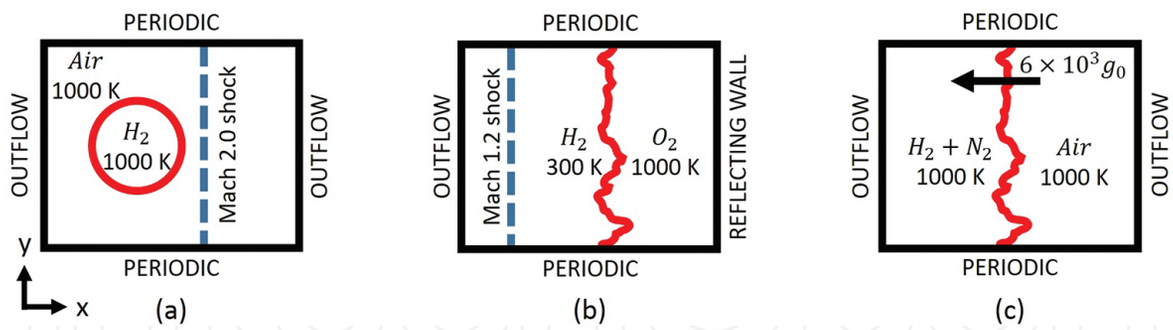

Figure 1. Schematic of (a) shock-bubble (b) Richtmyer-Meshkov and (c) Rayleigh-Taylor instabilities.

While the shock-bubble problem has illustrated certain key aspects of RM behaviour relevant to flames, the requirement to model controlled initial perturbations has led to recent numerical simulation studies in which shocks accelerate planar (premixed) flames subjected to well-defined (often sinusoidal) initial perturbations. For instance, Khokhlov et al. [37] investigated the growth of a *sinusoidally* perturbed premixed flame upon shock impingement and found the energy release from combustion varied in direct relation to the interfacial surface growth from the RM instability. These results are consistent with and follow from earlier numerical investigations of non-reacting RM interfaces [38] that found the interface surface area increased

in proportion to the baroclinic circulation deposition at the interface, according to the scaling relationship,

$$V \sim \Gamma_0 \left[c_1 \left(\frac{a_0}{\lambda} \right) + \frac{c_2}{\lambda} \right], \tag{1}$$

where V is the growth rate of the interfacial area, Γ_0 is the initial circulation, a_0 and λ are the perturbation amplitude and wavelength and c_1 and c_2 are non-dimensional coefficients. Eq. (1) points to a significant and thus far unrealized potential for mixing enhancement and improvements in combustion efficiency, particularly in a non-premixed configuration where the RM instability growth may be used to control and enhance the product formation at the interface. Thus, a configuration in which the shock impinges on an interface separating the fuel and oxidizer leading to a non-premixed flame that is controlled by turbulence and mixing at the interface (according to Eq. (1)) represents a significant departure from the earlier RM efforts described above. In Section 3, we describe results from our simulations involving a planar shock interacting with a planar, perturbed interface between fuel and oxidizer resulting in shock-induced non-premixed combustion. The details of the problem schematic are shown in **Figure 1(b)**.

The RM configurations discussed above are relevant to several applications in engineering and to a multitude of combustion phenomena occurring in nature. Shocks generated inside the combustion chamber of an internal combustion engine interact with flame or fuel/air interfaces of various thicknesses, and can result in the phenomenon of engine *knocking*, necessitating the use of expensive, higher octane fuels. In scramjet propulsion, mixing between fuel jets and co-flowing supersonic air can be impacted by the presence of oblique shocks and is thus central to the design of the injectors [39]. The baroclinic vorticity from the interaction has also been observed to play a crucial role in lifting the jet away from the combustor wall, thus decreasing wall heating effects [39]. The importance of accurately capturing such flow physics in realistic conditions was demonstrated recently in a proof-of-principle design and experimental study [40] of a shock-induced combustion ramjet (Schramjet). Our results (Section 3) below indicate a marked increase in the heat release rate and combustion efficiency immediately following shock impact, pointing the way towards high-performance combustion devices that can be manipulated by strategically structured shock trains.

We also discuss non-premixed combustion occurring at the site of a Rayleigh-Taylor unstable interface between fuel and oxidizer. The Rayleigh-Taylor instability occurs at a perturbed interface between fluids of different densities when the light fluid is accelerated into the heavier fluid (**Figure 1(c)**). Infinitesimal perturbations on the interface can still grow first exponentially (linear stage), and then secularly with a constant velocity (non-linear stage). When multiple modes are present, non-linear interactions are possible yielding an eventual turbulent, mixed state. RT-driven mixing afflicts a wide range of physical phenomena including energy yield in inertial confinement fusion [41], type Ia supernovae detonation [42–44], geophysical flows [45–47] and mixing in centrifugal combustors [8, 9, 48]. Although RT

http://dx.doi.org/10.5772/64746

instability in such flows is often intimately coupled with chemical/nuclear reactions and heat release, most studies have focused on the inert flow configuration. Recently, RT instability development in premixed flames [49, 50] has been investigated theoretically and numerically, although the corresponding non-premixed reacting configuration has never been studied before. Owing to its significance in a wide range of applications, the non-reacting RT instability has been extensively investigated over the last five decades [1, 21, 51–54]. From this body of work, a consensus has emerged on the dynamics of the turbulent RT mixing layer. When initialized with a broad spectrum of modes, the resulting flow has been observed to be self-similar, with the width of the mixing layer evolving quadratically in time according to [2, 3, 54–56]

$$h_{b/s} = aAgt^2, \tag{2}$$

where the subscripts b(s) refers to the advancing bubble(spike) front, respectively, g is the acceleration due to gravity, A is the Atwood number,

$$A = \frac{\rho_h - \rho_l}{\rho_h + \rho_l} \tag{3}$$

and α is the growth rate of the mixing layer.

Recently, RT dynamics has been recognized to play a central role in the performance of combustors that rely primarily on centrifugal loading. Recent innovations in gas turbine design include a shift towards the use of ultra-compact combustors (UCC) [8, 9] that operate at high g-loading. UCCs greatly reduce the weight of the gas turbine engine, thus increasing the thrust to weight ratio. In addition, the compact size allows for the inclusion of a reheat cycle between turbines, thus increasing the efficiency of the system. Most common UCC designs involve the admission of fuel and oxidizer streams tangentially into the combustor chamber, while the g-loading is provided centrifugally through high-speed rotation. Such a configuration in which a non-premixed fuel and oxidizer interface is subjected to high g-loading (~ 10^4 g_0) is susceptible to the development of the Rayleigh-Taylor (RT) instability [51, 52] at the flame site. In spite of this central role, the nature of the interaction between the RT instability and the flame surface has been poorly understood. RT-dominated flames provide unique opportunities in the design and operation of modern combustors that cannot be realized through device designs that rely primarily on shear-driven mixing to enhance combustion. For instance, in the unstable regime, RT growth will eventually outpace corresponding Kelvin-Helmholtz (KH) growth leading to greater mixing and more efficient burning. Thus, while RT grows self-similarly as ~ t^2, the shear-driven KH flows evolve as ~ t (but with a decaying centerline velocity). Correspondingly, the outer scale Reynolds number associated with RT mix (defined as $Re \equiv \frac{h\dot{h}}{\nu}$, where h(t) is the mixing layer width, $\dot{h}$ is its growth rate and ν is the mixture viscosity) will evolve as $\mathbf{t^3}$, while

remaining constant for KH flows [56]. This can allow for more compact designs of combustors, but also render unnecessary, several commonly used active and passive mixing augmenters. Furthermore, the faster growth of *Re* in RT ensures the flame does not undergo relaminarization upon ignition due to the increased viscosities, a common affliction that impacts several reacting flows. In addition, we have also discovered from preliminary numerical simulations that when the fuel stream is suitably diluted, the flame region can act as a stabilizing layer that can partially suppress the growth of the instability. This effect can be exploited in practical combustors to anchor the flame when necessary or to increase the time for the fuel to burn allowing for cleaner combustion with lesser unburnt fuel.

We describe detailed direct numerical simulations of non-premixed flames that evolve under the influence of mixing from RT or RM instabilities. Thus, the flow configurations studied here provide a simple, yet powerful framework in which to understand a wide class of non-premixed flames. The flame is initiated and sustained by the mixing process resulting directly from RT and RM instabilities, so that the combustion efficiency is directly dependent on the performance of these hydrodynamic instabilities. Similarly, RM/RT instability development is affected by heat release and the dynamics associated with the flame. Such a two-way coupling between flame and flow has been labelled Level III mixing, and anticipated in [5], but the non-premixed problems studied here provide a simple and idealized framework to examine such interactions.

2. Numerical methods and simulation details

The simulations reported in this chapter were performed using the FLASH code developed by the FLASH Center for Computational Sciences at the University of Chicago [57, 58]. FLASH is a multi-physics, finite-volume, Eulerian code with a broad range of capabilities including adaptive mesh refinement (AMR) on a block-structured mesh, state-of-the-art hydrodynamics solvers, implicit solvers for diffusion that include thermal conduction, mass diffusion and viscosity [57–59]. FLASH is also capable of operating in both ILES [60] (implicit large eddy simulation) and DNS [61] (direct numerical simulation) modes, where the former approach is suited to handle shocks and sharp interfaces [57, 58], while the latter approach is preferred in describing small-scale features in turbulence [61]. Recent modifications [62, 63] to the FLASH code by the authors have rendered it capable of describing a wide range of chemically reacting flows of relevance to combustion phenomena as they occur in realistic applications, and are summarized below, while additional details are available in refs. [57, 58, 62].

FLASH solves the compressible Euler equations (2)–(4), written in conservative form [57]

$$\frac{d\rho}{dt} + \nabla.\left(\rho V\right) = 0, \tag{4}$$

http://dx.doi.org/10.5772/64746

$$\frac{d\rho V}{dt} + \nabla.\left(\rho VV\right) + \nabla P = \rho g, \tag{5}$$

$$\frac{d\rho E}{dt} + \nabla.\left[\left(\rho E + P\right)V\right] = \rho V.g \tag{6}$$

where g, ρ, V, P and E are the gravitational acceleration, density, velocity, pressure and the total energy per unit mass, respectively. The internal energy (e) is obtained independently from the following equation:

$$\frac{d\rho e}{dt} + \nabla.\left[\left(\rho e + P\right)V\right] - V.\nabla P = 0. \tag{7}$$

Finally, pressure is updated using an ideal gas equation of state (EOS) for γ-law fluids. Reacting flows involving multiple species are handled through a separate advection equation for each species 'i' in the system given by,

$$\frac{\partial \rho Y_i}{\partial t} + \nabla.\left(\rho Y_i V\right) = 0 \tag{8}$$

where Y_i is the mass fraction of species 'i'. The hydro solver embedded in FLASH solves the governing equations using a second order PPM or fifth order WENO schemes. Diffusive transport of mass, momentum and heat are implemented through a dedicated diffuse unit that (a) implicitly updates the primary variable or (b) enforces the diffusion effects through the so-called "flux-based" infrastructure which updated the fluxes of primary variables.

Special care is given to the treatment of sharp interfaces and fronts to avoid spreading due to numerical diffusion. The details of the flame front thickness relative to the turbulent length scales are important in determining product formation in reacting flows. FLASH uses a multi-step approach to modify the underlying PPM/WENO methods in regions of large gradients in the primary field variables (density or temperature) to guard against the numerical diffusion of such features. The strategy involves artificial contact steepening [57, 58] using high-order polynomials of the zone-averaged primary variable in regions identified by the algorithm as having large third derivatives.

To enable FLASH to handle chemically reacting flows with heat addition, the EOS unit has been expanded to incorporate multiple species with temperature-dependent properties. The updated EOS covers a temperature range of 298 K to 5000 K and calculates thermodynamic properties by applying 10 coefficients for each species in the mixture. The 9 species 19 step reversible reaction mechanism of Mueller et al. [64] has been implemented to describe H_2-O_2

combustion. Viscosity and thermal conductivity were calculated using combination averaging formulas given in ref. [65].

Thus, the computational tools employed here are capable of handling a variety of physics including gas-phase chemical kinetics, diffusive transport of mass, momentum, and heat, shocks, presence of sharp interfaces, multi-species mixtures and thermal radiation. The results of an extensive validation and convergence study were reported in ref. [62] for several flows through comparison with analytical solutions, and published numerical and experimental data. Our validation cases included advection of reacting and non-reacting fronts in 1D and 2D [66], comparison with experimental data of laminar premixed flames in a Bunsen burner configuration [67, 68] and comparison with DNS of shock-driven combustion of a spherical bubble [69].

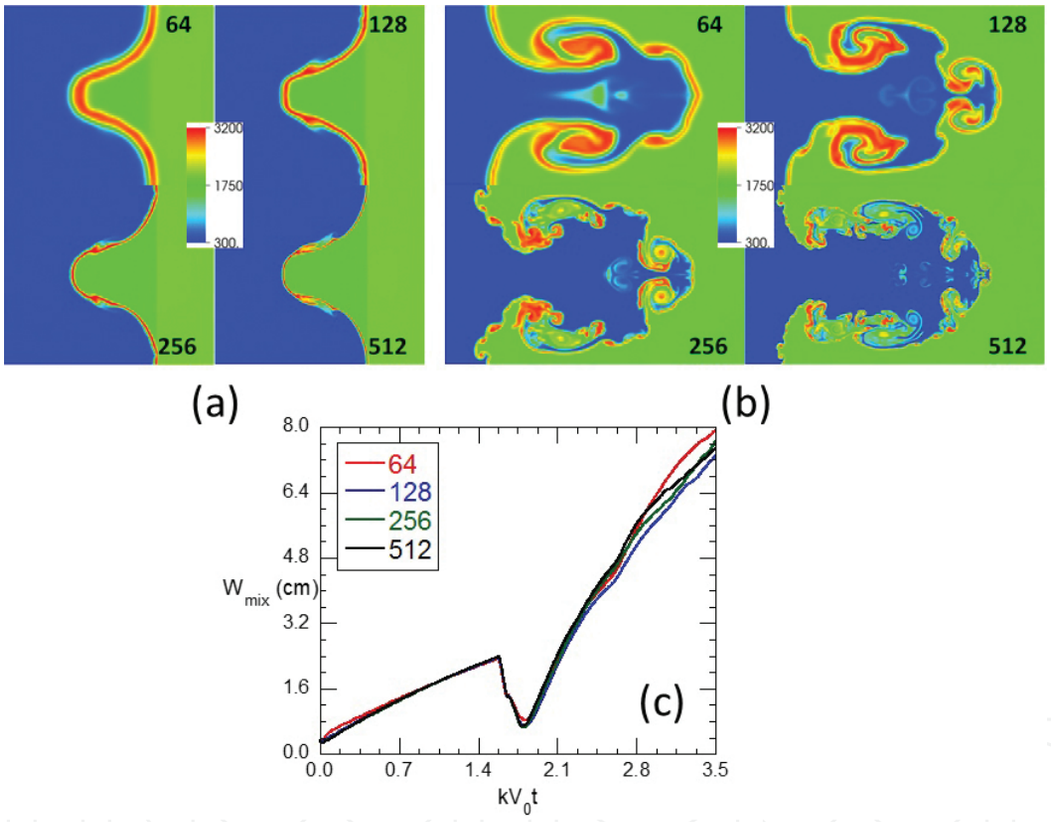

Figure 2. Temperature contours from simulations of a single-mode Richtmyer-Meshkov instability at a scaled time kV_0t = (a) 1.6 and (b) 3.0, at grid resolutions of 64 zones/λ, 128 zones/λ, 256 zones/λ and 512 zones/λ. (c) The corresponding width of the mixing zone is plotted against scaled time.

For all simulations reported here, detailed and systematic grid independence studies were performed. We summarize the results from one such study for the shock-accelerated RM problem described in Section 3. A sinusoidally perturbed (wavelength, $\lambda = 6$ cm), single-mode interface separating hydrogen (300 K) and oxygen (1625 K) was accelerated by a Mach 1.2 shock traversing from the light (H_2) to heavy (O_2) fluid (Atwood number = 0.5) in an aspect ratio 6 numerical shock tube (see [62] for details). The impulsive acceleration of the interface (ΔU)

http://dx.doi.org/10.5772/64746

triggers RM instability and the perturbed interface with initial amplitude ($h_0 = 0.2/k$, where $k = 2\pi/\lambda$) grows at a rate [11], $V_0 = \frac{dh}{dt} = kAh_0\Delta U$. The transmitted shock is reflected back from the end wall of the shock tube and interacts with the growing flame but this time processes a heavy-light interface at a scaled time kV_0t =1.6 (**Figure 2(a)**). Subsequently the interface undergoes a phase inversion followed by enhanced mixing due to the activation of higher harmonics and small-scale corrugations. **Figure 2** is a plot of temperature contours (a) before ($kV_0t = 1.6$) and (b) after ($kV_0t = 3.0$) reshock for grid resolutions of 64 zones/λ, 128 zones/λ, 256 zones/λ and 512 zones/λ. Simulations with zoning in excess of 64/λ are converged in terms of the gross features such as perturbation amplitude while the small-scale features retain some grid dependence as expected. In **Figure 2(c)** we plot the evolution of mixing width against scaled time for the four resolutions employed. Slight variations are observed at late times ($kV_0t > 3$), due to the appearance of small-scale, secondary instabilities which retain some grid dependence, while the amplitudes of penetration of the mixing layer have converged with respect to the grid resolution.

Finally, **Table 1** provides simulation details of the shock-bubble interaction problem, RM and RT instabilities.

	Domain size (cm)	Resolution	Mass diffusion	Thermal diffusion	Viscous diffusion
Shock-Bubble	3.0x1.5 ($x \times y$)	Uniform grid: 1280 × 640	Binary: $H_2 - O_2$	Combination averaging	Combination averaging
Richtmyer-Meshkov	36 × 6 × 6 ($x \times y \times z$)	Adaptive mesh: 1536 × 256 × 256	Numerical	Numerical	Numerical
Rayleigh-Taylor	24 × 8 × 8 ($x \times y \times z$)	Uniform grid: 768 × 256 × 256	Schmidt number = 0.75	Prandtl number = 0.75	Combination averaging

Table 1. Details of numerical simulations.

3. Results and discussion

An example of a typical configuration to investigate the interaction of a shockwave with a fuel bubble is shown in **Figure 1(a)**. In the numerical setup, a spherical hydrogen bubble moves towards and interacts with a stationary planar Mach 2 shock wave. The configuration for this 2D problem consists of a rectangular domain of dimensions 3 cm by 1.5 cm. The H_2 bubble diameter is 0.5 cm, while the stationary shock wave is located at $x = 0.7$. The hydrogen bubble approaches the shock with an ambient velocity U = 1.24e5 cm/s. The initial distance between the bubble surface and the shock is 0.2 mm, while the preshock temperature and pressure were specified to be 1000 K and 1 atm, respectively, for both air and hydrogen bubbles. The shocked

air on the left side of the domain is initialized with ambient velocity of $U_{shocked}$ = 4.3e4 cm/s, temperature of 1565 K and pressure of 4.4 atm. The mass fraction of the H_2 bubble as a function of radius is specified by [69]:

$$Y_{H_2} = \frac{1}{2}\left[1 + \tanh\left(\frac{r_c - r}{S}\right)\right] \tag{9}$$

$$r = \sqrt{\left(\left(x - x_0\right)^2 + \left(y - y_0\right)^2\right)} \tag{10}$$

where S represents the sharpness of the interface, r_c is the bubble radius and (x_0, y_0) determine the location of the bubble centre. As stated in ref. [62], S was chosen to be 3, which yields a value of 2.5e-2 cm for the initial interface thickness. As a result of the interaction between the shock wave and the bubble, shock waves travel towards the right outlet boundary at x=3 cm.

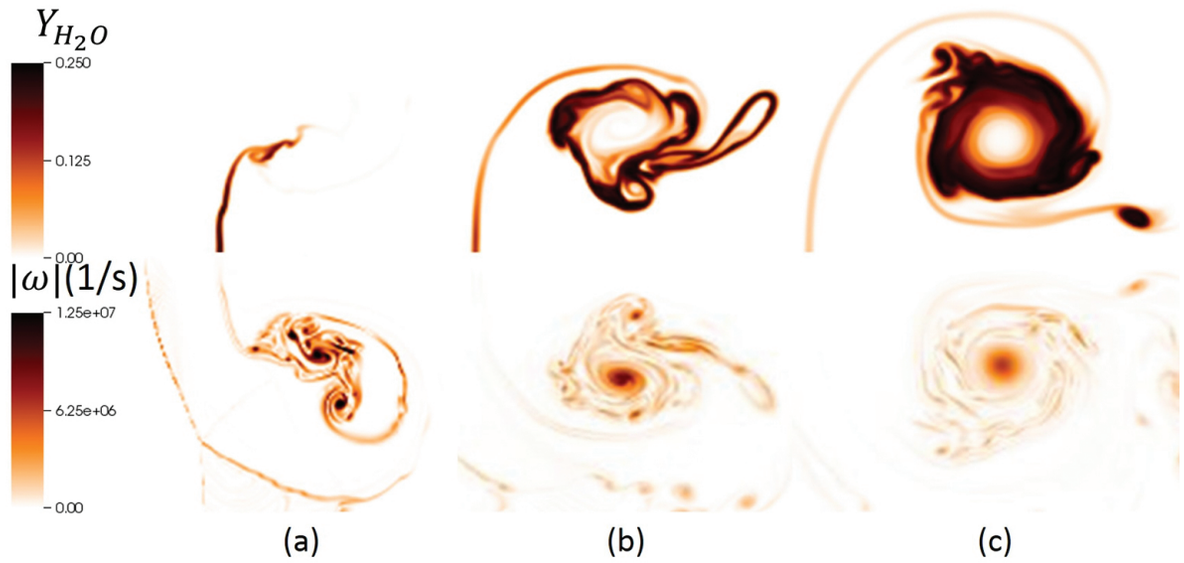

Figure 3. Time evolution of H_2O mass fraction (top panel) and magnitude of vorticity (bottom panel) from 2D simulations of a shock-bubble flame. Images are realized at t = (a) 10 μs, (b) 20 μs and (c) 40 μs.

Figure 3 shows contours of product (H_2O) mass fraction and magnitude of vorticity at different times in the evolution of the shocked fuel bubble. **Figure 3(a)** corresponds to 10 μs since shock impact and shows the onset of combustion has resulted in early product formation along the stem of the bubble. Vorticity contours reveal an organized vortex roll resulting from the baroclinic vorticity deposition from the shock interaction, and a counter-rotating counterpart (not shown). Thus, the bubble traverses under the induced velocity from the vortex ring. By t = 20 μs (**Figure 3(b)**), product formation is concentrated in a large reaction zone that is co-located with the vortex. The vorticity contour at this time shows the vorticity associated

http://dx.doi.org/10.5772/64746

with the primary rollup is now more organized in to a coherent structure. An interesting observation is that the product mass fraction appears to be concentrated along the rolled up vortex sheet, while the peaks of the vorticity are dominant within the core of the vortex structure. Thus, the reaction zones are concentrated along the rolled-up layers of vortex sheet that bring fuel and oxidizer surfaces into close contact, precipitating reaction and combustion. In contrast, the bulk of vorticity is concentrated in the vortex core and spreads from its peak value at this location due to diffusion. The images in **Figure 3(c)** correspond to $t = 40$ μs and show the distribution of vorticity has further diffused away from its peak value at the core. Contours of product mass fraction show the presence of H_2O has intensified within the outer layers of the vortex and is being sustained through a balance between production due to combustion and smearing due to mass diffusion.

We have investigated a variant of the RM instability, in which a planar shock interacts with a planar interface initially separating fuel and oxidizer streams. The advantage of this configuration is manifold and includes the ability to impose carefully formulated perturbations at the interface to control the progress of the turbulent mixing and the attendant flame dynamics. Furthermore, the simple geometry employed (absence of curvature effects found in the shock-bubble problem) implies that the flow is statistically isotropic and homogeneous in the two directions perpendicular to shock propagation. Thus, planar-averaged turbulent quantities may be represented as 1D functions in space and can be modelled using reduced-order 1D turbulence models.

We characterize the progress of the turbulent mixing in our simulations using the mixture fraction variable defined using [70]

$$Z = \frac{\left(\frac{Z_H}{2W_H} + \frac{Z_{O_a} - Z_O}{W_O}\right)}{\left(\frac{Z_{H_f}}{2W_H} + \frac{Z_{O_a}}{W_O}\right)}, \tag{11}$$

$$Z_H = W_H\left(\frac{2\Upsilon_{H_2}}{W_{H_2}} + \frac{\Upsilon_H}{W_H} + \frac{2\Upsilon_{H_2O}}{W_{H_2O}} + \frac{\Upsilon_{OH}}{W_{OH}} + \frac{\Upsilon_{HO_2}}{W_{HO_2}} + \frac{2\Upsilon_{H_2O_2}}{W_{H_2O_2}}\right),$$

$$Z_O = W_O\left(\frac{2\Upsilon_{O_2}}{W_{O_2}} + \frac{\Upsilon_O}{W_O} + \frac{\Upsilon_{H_2O}}{W_{H_2O}} + \frac{\Upsilon_{OH}}{W_{OH}} + \frac{2\Upsilon_{HO_2}}{W_{HO_2}} + \frac{2\Upsilon_{H_2O_2}}{W_{H_2O_2}}\right)$$

where Z_i, W_i and Υ_i are the mixture fraction, molecular weight and mass fraction of species 'i', while Z_{O_a} and Z_{H_f} are the atomic mixture fraction of O and H evaluated in the air and fuel streams, respectively.

The mixture fraction defined from Eq. (11) is a conserved quantity in our reacting flow simulations and also remains monotonic across the mixing layer enabling a direct comparison

between the reacting and non-reacting flow simulations (quantities such as mass fractions are non-monotonic in reacting flows and cannot be used for this purpose). For instance, the x-locations of the 1 and 99% levels of the planar-averaged mixture fraction <Z> can be indicative of the extents of the mixing layer width and can be tracked in time to evaluate the growth rate of the turbulent mixing layer in both reacting and non-reacting flows. The initial interface is seeded by perturbations dominated by short wavelengths [3] and given by

$$h(y,z,t=0)=\sum_{k_y,k_z}\begin{bmatrix} a_k\cos(k_y y)\cos(k_z z)+ \\ b_k\sin(k_y y)\cos(k_z z)+ \\ c_k\cos(k_y y)\sin(k_z z)+ \\ d_k\sin(k_y y)\sin(k_z z) \end{bmatrix} \tag{12}$$

In our simulations, we evaluate Eq. (12) for an annular spectrum of wavenumbers (k_y, k_z) ranging from modes 16–32. We scale time according to $\tau = t\frac{A^+U}{\lambda_{min}}$, where $\lambda_{\min}$ is the shortest wavelength in the initial condition packet, U is the jump velocity acquired by the initially stationary interface as a result of shock impact (obtained from Rankine-Hugoniot jump conditions) and A^+ is the Atwood number across the mixing layer corresponding to post-shock conditions. The schematic details for the multimode RM problem are shown in **Figure 1(b)** and show the variegated interface separating fuel (H_2 at 300 K) and oxidizer (O_2 at 1000 K). The planar shock is initialized in the fuel stream, with a shock strength corresponding to Ma 1.2. Thus, the shock proceeds from a light to heavy fluid, so that the Atwood number is positive and is ~ 0.66. The impedance mismatch of the fluids involved in such an interaction is expected to result in reflected and transmitted shocks, which are processed by the outflow and reflecting boundary conditions, respectively. Thus, the transmitted shock from the first interaction is reflected from the endwall and is incident on the interface a second time. However, during this 'reshock' event, the 'incident' shock proceeds now from the heavy fluid (shocked O_2) to a light fluid (shocked H_2), so that the Atwood number for this interaction is −0.72. The heavy-to-light interaction produces a second transmitted shock in the H_2 stream, and a reflected rarefaction wave in the O_2 stream.

In **Figure 4(a,b)**, we show iso-surfaces of mixture fraction ranging from 1 to 99% at two critical instances in the evolution of the RM flame: early time following the first shock interaction (**Figure 4(a)**) and late time following the reshock event (**Figure 4(b)**). The iso-surfaces are coloured to indicate temperature variations across the mixing layer. At early time (τ = 16), dominant structures on the flamefront appear to be shorter in wavelength and are driven primarily by the baroclinic vorticity from the shock impact. The growth of these modes is also enhanced by a combustion wave that is generated during ignition, which accelerates the mixing front, while the pressure gradient associated with the expansion wave drives mode growth consistent with a short-lived variable-g RT phase. Across the mixing layer, regions of high temperature are visible and are predominantly organized as bubble and spike structures penetrating through the flame region. The maximum temperature is observed closer to the

http://dx.doi.org/10.5772/64746

stoichiometric surface and approaches ~3200 K, the expected adiabatic flame temperature for H_2–O_2 combustion.

At the late time (τ = 160) shown in **Figure 4(b)**, the mixing region has been subjected to a second shock (the reshock event from the reflected shock) and shows the second shock has significantly transferred energy to large-scale structures. The initial condition for this second shock event is comprised of modes (structures) that are already non-linear and thus have saturated amplitudes. Thus the reshock event constitutes a finite-amplitude initialization of the RM instability, resulting in aggressive growth of already mature modes. This outcome is of consequence to the performance of scramjet engines which can be designed to expose the flame/mixing layer to multiple shock events, strategically positioned to maximize mixing and combustion efficiency, with the growth of the instability becoming more aggressive with each shock event. Temperature variations across the mixing layer at τ = 160 are consistent with the presence of large-scale structures and are found to be organized with the dominant bubble and spike structures that penetrate the mixing layer and flame regions.

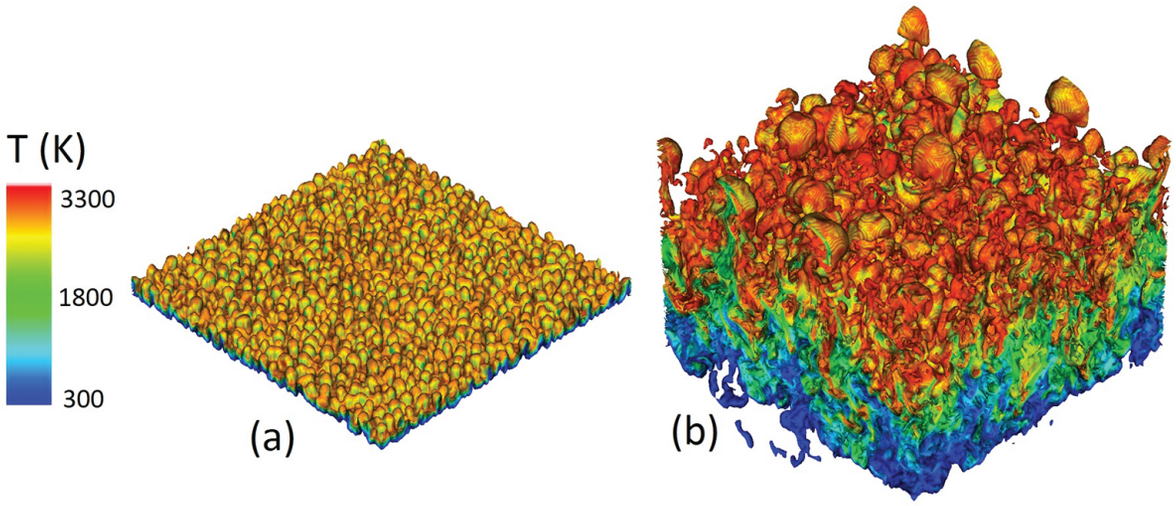

Figure 4. Time evolution of iso-surfaces of Z and the temperature distribution in the RM-driven flame (a) shortly after incident shock (τ= 16) and (b) at late time after the reshock (τ= 160).

We provide quantitative data from our reshocked RM simulation in **Figure 5**. The flame surface area was computed using a 3D numerical surface computation algorithm in the VisIt-2.9 software [71, 72] and is shown in **Figure 5** as a function of the non-dimensional RM time τ. When scaled with the square of the lateral shock tube dimension (L), the flame surface area shows significant increases shortly after the shock events at $\tau \approx 0$ and $\tau \approx 80$. In between these events, the surface area growth is gradual and consistent with the underlying power-law behaviour of the mixing layer width. Note that the surface area of the mixing layer is affected not just by the large scales (which develop as t^{θ}), but significantly by the presence of small-scale features which can be affected by diffusion and flame polishing. We

intend to examine these effects in detail in follow-up articles. In **Figure 5**, we also show the time evolution of the integrated heat release rate defined according to

$$\int_0^{L_x} < \dot{e}_{comb.} > dx, \tag{13}$$

where L_x and $\dot{e}_{comb}$ are length of computational domain in x-direction and heat release rate while the operator $< \bullet >$ indicates planar averaging in y-z direction. Peaks in the heat release rate correspond to significant ignition events that follow both the first and second shocks. Comparatively very little heat release is observed between such events.

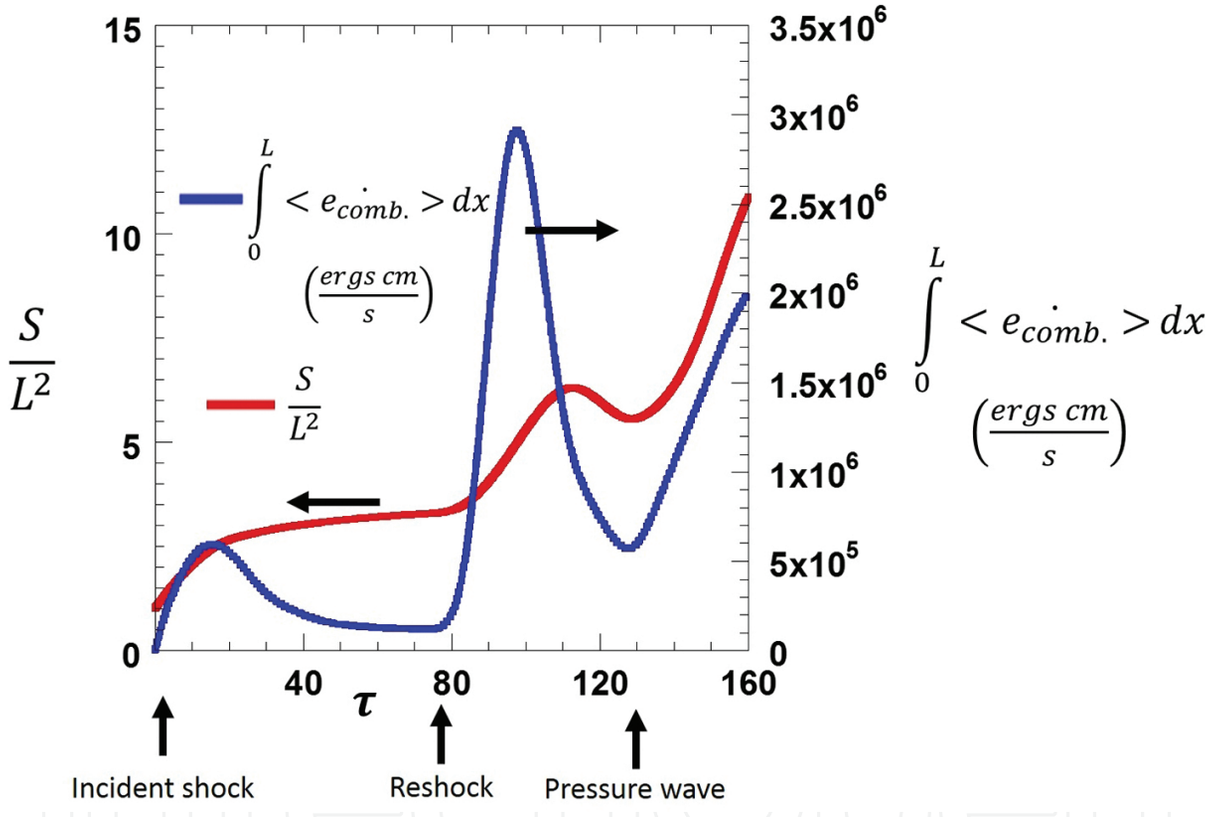

Figure 5. Evolution of flame surface area and integral heat release rate versus scaled time $\tau = t\frac{A^+U}{\lambda_{min}}$ from RM simulation.

We also discuss our recent results of the reacting Rayleigh-Taylor instability in a non-premixed flame setting. We present results from high resolution, Navier-Stokes simulations of a chemically reacting RT unstable interface separating hydrogen (fuel) and air under strong acceleration ($g = 6 \times 10^3\, g_0$, where $g_0 = -981\ cm/s^2$), representative of conditions in ultra-compact combustion devices [8, 9]. The density ratio across the interface corresponds to an Atwood number of 0.6, while the temperature on the fuel and air side were specified uniformly to be 1000 K. Note that in our simulations, the fuel stream (H_2) was diluted with N_2, so that the

http://dx.doi.org/10.5772/64746

Atwood number and hence the density contrast driving the instability could be easily varied by adjusting the concentration of N_2. The simulations were initialized with a narrow spectrum of perturbation modes imposed at the interface, leading eventually to self-similarity and turbulence. A uniform grid (256 zones/L) was employed such that $\Delta x \sim \eta$ (Kolmogorov length scale) is sufficient to resolve [73, 74] late time turbulent flow field.

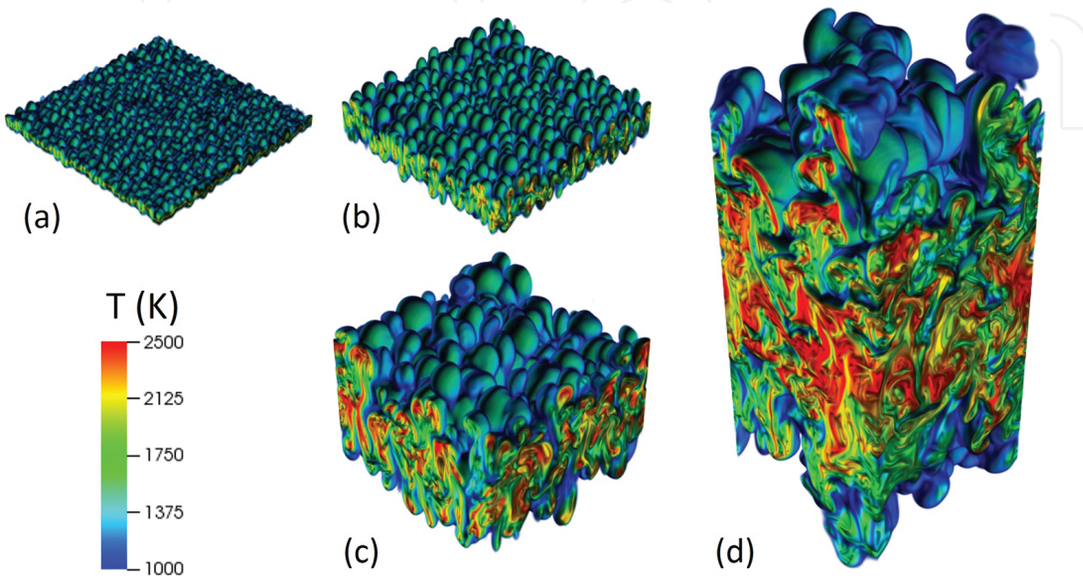

Figure 6. Time evolution of reacting RT instability at Agt^2/L = (a) 0.3, (b) 1.2, (c) 4.8 and (d) 19.2.

In **Figure 6**(**a**–**d**), we plot qualitative images from different stages of our reacting RT simulation, in a non-premixed configuration. The images show iso-surfaces of the mixture fraction Z (defined according to Eq. (11)), coloured by temperature. Note that for this fuel-oxidizer combination, and conditions investigated here, the flame sheet corresponds to Z ~ 12%, the stoichiometric iso-surface of mixture fraction. The timestamps are identified in terms of the RT-characteristic non-dimensional timescale Agt^2/L, where L is the spanwise extent of the computational domain. Through **Figure 6**(**a**–**d**), there is a clear progression in the development of RT to larger scales at the bubble and spike front. This is accompanied by ignition and combustion that results from the turbulent mixing process, and in turn affects it. The appearance of high temperature regions is visible within the internal layers of the turbulent mixing region, so that at late times, the flame sheet appears highly convoluted at both the large and small scales. The peak temperature within the RT mixing layer consistently reaches ~ 2500 K, approaching the adiabatic flame temperature for H_2-air combustion of ~2600.

In **Figure 7**, we plot quantitative data corresponding to the integral heat release rate and the total flame sheet surface area from our turbulent RT flame simulations. Interestingly, we find both quantities to scale with the characteristic non-dimensional timescale of the problem Agt^2/L. The heat release rate displays an early spike, corresponding to the first instance of ignition, likely caused due to diffusion across the initial interface. This is followed by a short-lived period during which both the heat release rate and the surface area grow rapidly in

response to the linear growth of perturbation modes imposed on the surface. However, following non-linear saturation and the onset of self-similarity (Agt^2/L ~ 3–5), an asymptotic growth rate is observed which appears to scale quadratically in time. We expect the surface area to be influenced by the square of the dominant wavelength $<\lambda>$ that deform the interface at any time, but also by intermediate scales such as the square of the Taylor microscales [1].

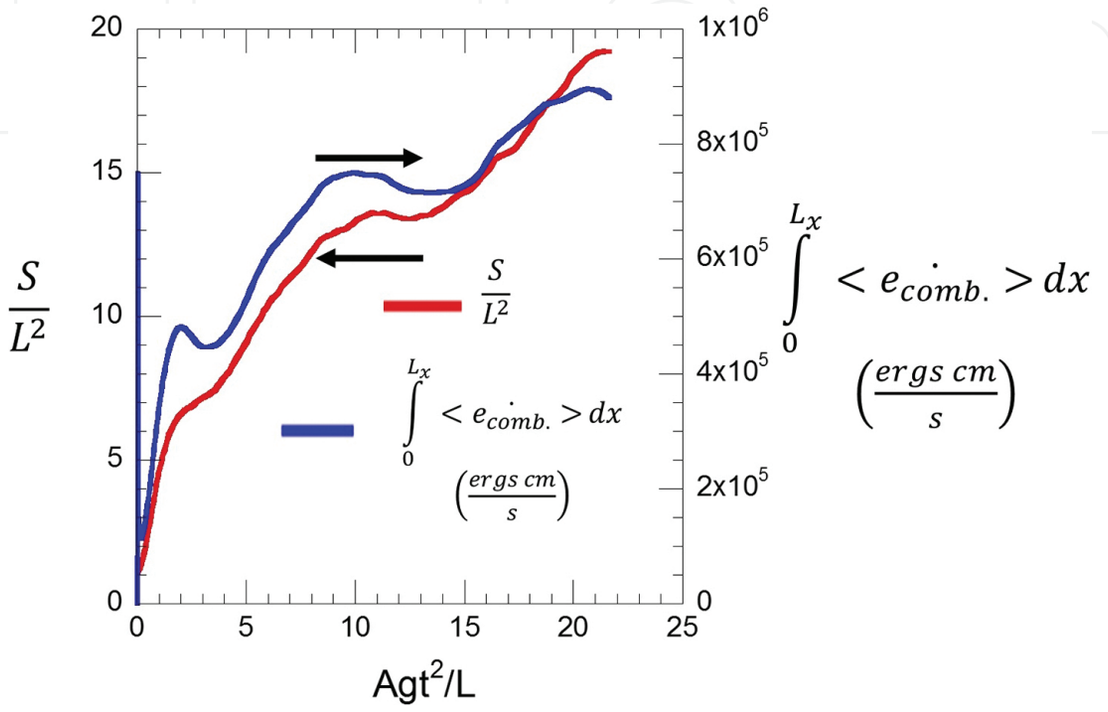

Figure 7. Evolution of flame surface area and integral heat release rate against Agt^2/L from reacting RT simulation.

4. Summary

In this chapter, we have reviewed historical progress and recent results in the area of combustion processes occurring in interfacial instabilities. While earlier efforts have focused on combustion associated with shear-driven instabilities (KH), the significance of baroclinically driven RM and buoyancy-driven RT instabilities to several combustor designs is gaining recognition. We have investigated these flows in a non-premixed setting using direct numerical simulations. Both RM and RT instabilities allow for aggressive growth and control of the combustion process through the turbulent mixing they engender between the fuel and oxidizer layers. In RM, the mixing can be controlled through several factors including the Atwood number, initial perturbations imposed at the interface and most significantly by reshocking the mixing layer at strategically chosen times. Similarly, the RT mixing and combustion can be manipulated through the Atwood number by modifying the level of N_2 dilution in the fuel stream. This is an effective strategy, since the N_2 is inert and does not affect the reaction kinetics, but can significantly alter the hydrodynamic mixing dynamics through the Atwood number.

The aggressive mixing and turbulence associated with these flows is beneficial since it can act to counter/delay the relaminarization process commonly observed in shear-driven flames due to increased viscosity following ignition. To address some of the above issues, we have defined novel formulations of RT and RM non-premixed combustion that can serve as canonical problems for this class of flows. The statistical isotropy and homogeneity in the plane of the interface implies the planar-averaged quantities associated with these flows can be represented as 1D functions, and thus can be used readily in reduced order turbulent combustion models. Our simulations also track quantities of interest to the turbulent combustion community such as the heat release rate and flame surface area, revealing a rich and complex array of phenomena associated with those quantities.

Acknowledgements

FLASH was developed by the DOE-sponsored ASC/Alliance Center for Astrophysical Thermonuclear Flashes at the University of Chicago. This research used resources of the Argonne Leadership Computing Facility, which is a DOE Office of Science User Facility supported under Contract DE-AC02-06CH11357.

Author details

Praveen Ramaprabhu*, Nitesh Attal and Hilda Varshochi

*Address all correspondence to: pramapra@uncc.edu

University of North Carolina at Charlotte, Charlotte, NC, USA

References

[1] W. H. Cabot and A. W. Cook, Nat. Phys. 2, 562 (2006).

[2] P. Ramaprabhu, V. Karkhanis, and A. G. W. Lawrie, Phys. Fluids 25, 115104 (2013).

[3] G. Dimonte *et al.*, Phys. Fluids 16, 1668 (2004).

[4] A. A. Gowardhan and F. F. Grinstein, J. Turbulence 12, 1 (2011).

[5] P. E. Dimotakis, Annu. Rev. Fluid Mech. 37, 329 (2005).

[6] S. B. Pope, *Turbulent flows* (Cambridge University Press, Cambridge, England, 2000).

[7] M. K. Smart, N. E. Hass, and A. Paull, AIAA J. 44, 2366 (2006).

[8] J. Zelina, D. T. Shouse, and R. D. Hancock, *ASME Turbo Expo 2004: Power Land, Sea, and Air* (ASME, Vienna, Austria, 2004), p. 53.

[9] D. Blunck *et al*., *ASME Turbo Expo 2013: Turbine Tech. Conf. Exposition* (ASME, San Antonio, Texas, 2013), p. V01AT04A026.

[10] K. R. McManus, U. Vandsburger, and C. T. Bowman, Combust. Flame 82, 75 (1990).

[11] R. D. Richtmyer, Commun. Pure Appl. Math. 13, 297 (1960).

[12] E. E. Meshkov, Izv. Acad. Sci. USSR Fluid Dynamics 4, 101 (1969).

[13] M. Brouillette, Annu. Rev. Fluid Mech. 34, 445 (2002).

[14] N. J. Zabusky, Annu. Rev. Fluid Mech. 31, 495 (1999).

[15] S. Zhang, G. Peng, and N. J. Zabusky, J. Turbulence 6, 1 (2005).

[16] J. M. Picone and J. P. Boris, J. Fluid Mech. 189, 23 (1988).

[17] J. G. Wouchuk and K. Nishihara, Phys. Plasmas 4, 1028 (1997).

[18] S.-I. Sohn, Phys. Rev. E 67, 026301 (2003).

[19] V. N. Goncharov, Phys. Rev. Lett. 88, 134502 (2002).

[20] B. Thornber, D. Drikakis, and D. Youngs, Comput. Fluids 37, 867 (2008).

[21] D. L. Youngs, Laser Part. Beams 12, 725 (1994).

[22] S. K. Shankar, S. Kawai, and S. K. Lele, Phys. Fluids 23, 024102 (2011).

[23] B. Thornber, D. Drikakis, D. L. Youngs, and R. J. R. Williams, J. Fluid Mech. 654, 99 (2010).

[24] F. F. Grinstein, A. A. Gowardhan, and A. J. Wachtor, Phys. Fluids 23, 034106 (2011).

[25] G. Dimonte, G. Terrones, F. J. Cherne, and P. Ramaprabhu, J. Appl. Phys. 113, 024905 (2013).

[26] D. Ranjan, J. Niederhaus, B. Motl, M. Anderson, J. Oakley, and R. Bonazza, Phys. Rev. Lett. 98, 024502 (2007).

[27] B. J. Balakumar, G. C. Orlicz, C. D. Tomkins, and K. P. Prestridge, Phys. Scr. 2008, 014013 (2008).

[28] J. Kane, D. Arnett, B. A. Remington, S. G. Glendinning, G. Bazan, R. P. Drake, and B. A. Fryxell, Astrophys. J. Suppl. Ser. 127, 365 (2000).

[29] B. D. Collins and J. W. Jacobs, J. Fluid Mech. 464, 113 (2002).

[30] C. Tomkins, S. Kumar, G. Orlicz, and K. Prestridge, J. Fluid Mech. 611, 131 (2008).

[31] G. H. Markstein, *Nonsteady Flame Propagation* (Pergamon, Oxford, 1964).

[32] M. Gui, B. Fan, G. Dong, and J. Ye, Shock Waves 18, 487 (2009).

[33] Y. Ju, A. Shimano, and O. Inoue, in *Symp. (Int.) Combust*. (Elsevier, Boulder, Colorado, USA, 1998), pp. 735.

[34] G. A. Batley, A. C. McIntosh, and J. Brindley, Proc. R. Soc. London Ser. A 452, 199 (1996).

[35] H. H. Teng, Z. L. Jiang, and Z. M. Hu, Acta Mech. Sin. 23, 343 (2007).

[36] N. Haehn, D. Ranjan, C. Weber, J. Oakley, D. Rothamer, and R. Bonazza, Combust. Flame 159, 1339 (2012).

[37] A. M. Khokhlov, E. S. Oran, A. Y. Chtchelkanova, and J. C. Wheeler, Combust. Flame 117, 99 (1999).

[38] V. Kilchyk, R. Nalim, and C. Merkle, J. Fluids Eng. 135, 031203 (2013).

[39] J. Yang, T. Kubota, and E. E. Zukoski, AIAA J. 31, 854 (1993).

[40] R. G. Veraar, A. E. H. J. Mayer, J. Verreault, R. A. Stowe, R. Farinaccio, and P. G. Harris, *16th AIAA/DLR/DGLR Int. Space Planes Hypersonic Syst. Technol. Conf*. (Bremen, Germany, 2009), p. 8.

[41] J. D. Lindl, *Inertial Confinement Fusion: The Quest for Ignition and Energy Gain Using Indirect Drive* (Springer-Verlag, New York, 1998).

[42] M. Zingale, S. E. Woosley, C. A. Rendleman, M. S. Day, and J. B. Bell, Astrophys. J. 632, 1021 (2005).

[43] M. Herant, W. Benz, W. R. Hix, C. L. Fryer, and S. A. Colgate, Astrophys. J. 435, 339 (1994).

[44] C.-Y. Wang and R. A. Chevalier, Astrophys. J. 549, 1119 (2001).

[45] S. Zhong and M. T. Zuber, Earth Planet. Sci. Lett. 189, 75 (2001).

[46] B. D. Marsh and I. S. E. Carmichael, J. Geophys. Res. 79, 1196 (1974).

[47] C. S. Huang, M. C. Kelley, and D. L. Hysell, J. Geophys. Res. 98, 15631 (1993).

[48] W. A. Sirignano, D. Dunn-Rankin, F. Liu, B. Colcord, and S. Puranam, AIAA J. 50, 1645 (2012).

[49] A. Petchenko, V. Bychkov, V. Akkerman, and L.-E. Eriksson, Phys. Rev. Lett. 97, 164501 (2006).

[50] M. Chertkov, V. Lebedev, and N. Vladimirova, J. Fluid Mech. 633, 1 (2009).

[51] L. Rayleigh, *Scientific Papers II* (Cambridge University Press, Cambridge, England, 1900).

[52] G.I.Taylor, Proc. R. Soc. London, Ser. A 201, 192 (1950).

[53] G. Dimonte and M. Schneider, Phys. Rev. E 54, 3740 (1996).

[54] S. B. Dalziel, P. F. Linden, and D. L. Youngs, J. Fluid Mech. 399, 1 (1999).

[55] P. Ramaprabhu, G. Dimonte, and M. J. Andrews, J. Fluid Mech. 536, 285 (2005).

[56] P. Ramaprabhu and M. J. Andrews, J. Fluid Mech. 502, 233 (2004).

[57] B. Fryxell *et al*., Astrophys. J. Suppl. Ser. 131, 273 (2000).

[58] Flash User's Guide (University of Chicago) http://flash.uchicago.edu/site/flashcode/user_support/.

[59] A. Dubey, K. Antypas, M. K. Ganapathy, L. B. Reid, K. Riley, D. Sheeler, A. Siegel, and K. Weide, Parallel Comput. 35, 512 (2009).

[60] F. F. Grinstein, L. G. Margolin, and W. J. Rider, *Implicit Large Eddy Simulation: Computing Turbulent Fluid Dynamics* (Cambridge University Press, New York, 2010).

[61] P. Moin and K. Mahesh, Annu. Rev. Fluid Mech. 30, 539 (1998).

[62] N. Attal, P. Ramaprabhu, J. Hossain, V. Karkhanis, M. Uddin, J. R. Gord, and S. Roy, Comput. Fluids 107, 59 (2015).

[63] N. Attal and P. Ramaprabhu, Shock Waves 25, 307 (2015).

[64] M. A. Mueller, T. J. Kim, R. A. Yetter, and F. L. Dryer, Int. J. Chem. Kinet. 31, 113 (1999).

[65] S. Mathur, P. K. Tondon, and S. C. Saxena, Mol. Phys. 12, 569 (1967).

[66] G. Billet and R. Abgrall, Comput Fluids 32, 1473 (2003).

[67] X. Zhou, G. Brenner, T. Weber, and F. Durst, Int. J. Heat Mass Transfer 42, 1757 (1999).

[68] Q. V. Nguyen, R. W. Dibble, C. D. Carter, G. J. Fiechtner, and R. S. Barlow, Combust. Flame 105, 499 (1996).

[69] G. Billet, V. Giovangigli, and G. de Gassowski, Combust. Theor. Model. 12, 221 (2008).

[70] R. W. Bilger, in *Symp. (Int.) Combust*. (Elsevier, Pittsburgh, Pennsylvania, USA, 1989), pp. 475.

[71] E. W. Bethel, H. Childs, and C. Hansen, *High Performance Visualization: Enabling Extreme-Scale Scientific Insight* (CRC Press, Boca Raton, Florida, USA, 2012).

[72] VisIt, (Lawrence Livermore National Laboratory) http://www.llnl.gov/visit.

[73] J. H. Chen, Proc. Combust. Inst. 33, 99 (2011).

[74] R. Yu, X.-S. Bai, and A. N. Lipatnikov, J. Fluid Mech. 772, 127 (2015).